Available online at www.sciencedirect.com

SciVerse ScienceDirect

Geochimica et Cosmochimica Acta 89 (2012) 240–255

Geochimica et Cosmochimica Acta

www.elsevier.com/locate/gca

Seasonal resolution of Eastern Mediterranean climate change since 34 ka from a Soreq Cave speleothem

Ian J. Orland [a,*], Miryam Bar-Matthews [b], Avner Ayalon [b], Alan Matthews [c], Reinhard Kozdon [a], Takayuki Ushikubo [a], John W. Valley [a]

[a] WiscSIMS, Department of Geoscience, University of Wisconsin, 1215 W Dayton St., Madison, WI 53706, USA
[b] Geological Survey of Israel, 30 Malchei Israel St., Jerusalem 95501, Israel
[c] The Institute of Earth Sciences, The Hebrew University, Givat Ram, Jerusalem 91904, Israel

Received 21 October 2011; accepted in revised form 15 April 2012; available online 21 April 2012

Abstract

The combination of ion microprobe analysis of $\delta^{18}O$ and confocal laser fluorescent microscope imaging of annual growth bands in a Soreq Cave speleothem provides sub-annual-scale climate information between 34 and 4 ka. This high-resolution methodology is ideal both for comparing seasonal climate patterns across broad windows of time and examining rapid climate events, such as the Younger Dryas termination, in detail. The sub-annual $\delta^{18}O$ gradients we report represent a combination of seasonal variability in rainfall amount and air temperature. A distinct change in both the pattern of fluorescent banding and the gradient of $\delta^{18}O$ measured *in situ* across single, annual growth bands indicates a change in seasonal climate patterns of the Eastern Mediterranean region following Heinrich event 1 and again after the Younger Dryas. Throughout the Holocene, wet winters and dry summers characterized regional climate. During the Younger Dryas, we find that regional climate may have been more arid than in the Holocene, but the fluorescent banding pattern indicates that the supply of dripwater to the cave was more consistent year-round. We suggest that a reduced gradient of seasonal precipitation, occasional snowfall, and vegetation differences may have all contributed to the isotope and fluorescent banding patterns observed during Heinrich event 1 and the last glacial stadial. Detailed investigation of the Younger Dryas termination reveals a rapid onset of regional environmental change. Fluorescent band counting indicates that the Younger Dryas termination, as recorded by rainfall in the Eastern Mediterranean, spanned a minimum of 12 years.

1. INTRODUCTION

1.1. Background

Model predictions of climate change over the next century are in broad agreement with respect to globally averaged surface temperatures, showing an increase of ~2–4 °C given projected greenhouse gas emissions, but key details remain uncertain (IPCC, 2007). Likewise, models predict a climate response that varies by both region and rate. It follows that high-resolution proxy records of past climate events are essential for calibrating model forecasts of seasonal and abrupt climate change on both regional and global scales. In this paper, we present a high-resolution

Abbreviations: CLFM, confocal laser fluorescent microscopy; EM, Eastern Mediterranean; LGM, last glacial maximum; H1, Heinrich event 1; S1, Sapropel event 1; YD, Younger Dryas

* Corresponding author. Tel.: +1 608 262 8960; fax: +1 608 262 0693.
E-mail addresses: orland@geology.wisc.edu (I.J. Orland), matthews@gsi.gov.il (M. Bar-Matthews), ayalon@gsi.gov.il (A. Ayalon), alan@vms.huji.ac.il (A. Matthews), rkozdon@geology.wisc.edu (R. Kozdon), ushi@geology.wisc.edu (T. Ushikubo), valley@geology.wisc.edu (J.W. Valley).

0016-7037/$ - see front matter © 2012 Elsevier Ltd. All rights reserved.
http://dx.doi.org/10.1016/j.gca.2012.04.035

geochemical climate proxy from a cave deposit in the Eastern Mediterranean (EM) region that is a record of seasonal precipitation from 34 to 4 ka. Combined with data presented in Orland et al. (2009), we build a regional record of seasonal climate from 34 to 1 ka.

Cave deposits (speleothems) are valuable records of multiple paleoclimate variables in numerous locations around the globe (e.g., Baker et al., 1993; Wang et al., 2001; McDermott, 2004; Fairchild et al., 2006; Baldini et al., 2008; Cheng et al., 2009; Lachniet, 2009; Wong et al., 2011). In many cases, geochemical tracers in speleothems are used to identify changes in global and regional climate trends on a decadal to millennial scale. Given conventional drill-sampling techniques (mm-scale spatial resolution) and typical speleothem growth rates, however, most speleothem-based proxy studies from semi-arid climates are unable to resolve seasonal or sub-annual information. Following the methodology established by Orland et al. (2009), this study examines the utility of *in situ* micron-scale (sub-annual temporal resolution) ion microprobe oxygen isotope ($\delta^{18}O$) analysis for interpreting seasonal climate patterns in a Soreq Cave (Israel) stalactite ("sample 2N", Fig. 1) that grew during the last glacial period, deglaciation and Holocene.

1.2. Related environmental proxy records

The record of seasonal climate from this study represents new information for interpreting mid-latitude climate dynamics during Northern Hemisphere deglaciation. Speleothem sample 2N provides a relevant record of both regional- and hemisphere-scale climate responses to deglaciation (Bar-Matthews et al., 1999, 2000, 2003). The existing $\delta^{18}O$ record from Soreq Cave generally agrees with that of other

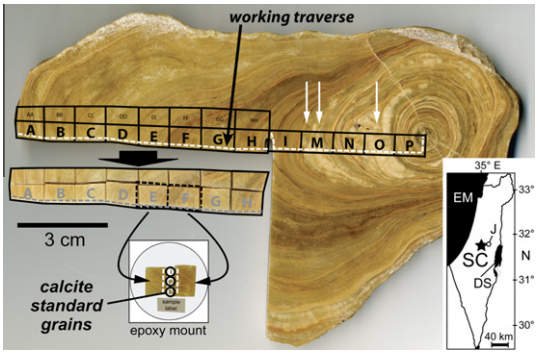

Fig. 1. Stalactite sample 2N from Soreq cave, Israel, cut in horizontal cross-section. Samples from the matching face were drilled for geochronology (Table 1). The "working traverse" for ion microprobe analysis of $\delta^{18}O$ is highlighted with a white dashed line and the location of the 1 cm cubes (A–P) cut for ion microprobe mounts are outlined in black. Areas of irregular calcite crystal growth, indicated by white arrows, are visible in cubes M, N, and O. Inset, left: picture of a 25 mm round epoxy mount for ion microprobe analysis with cubes E and F positioned with the working traverse centered and UWC-3 calcite standard grains in the middle. Inset, right: map of Israel showing the location of Soreq Cave (SC), Jerusalem (J), the Eastern Mediterranean Sea (EM) and the Dead Sea (DS).

speleothems in the region (Frumkin et al., 2000; Verheyden et al., 2008). Soreq Cave is located such that it is influenced by the eastward advection of complex climatic variability in the North Atlantic. Further, the Soreq Cave isotope record may respond indirectly to an enhanced African Monsoonal System (Almogi-Labin et al., 2004, 2009) and movement of the Intertropical Convergence Zone, a major climate teleconnection mechanism examined and invoked by many paleoclimate workers (Wang et al., 2006; Anderson et al., 2009; Cheng et al., 2009; Waldmann et al., 2010; Denton et al., 2010).

Nearby regional paleoclimate records include lake level, marine sediment, and pollen environmental proxies. Shoreline sediments from the Dead Sea, which is in a terminal basin ~45 km east of Soreq Cave, are used to reconstruct paleo-Dead Sea levels and regional water balance (Enzel et al., 2003; Bartov et al., 2003; Bookman et al., 2004; Lisker et al., 2009; Torfstein et al., 2009; Stein et al., 2010; Waldmann et al., 2010). Understanding the contributions of both precipitation and evaporation is imperative for interpreting Dead Sea levels; since this is ambiguous in Dead Sea shoreline records, the interpretation of past regional rainfall amount is uncertain. Curiously, however, Dead Sea level is highest during the last ice age when high $\delta^{18}O$ values in Soreq Cave speleothems are interpreted by Bar-Matthews et al. (1997, 2003) to indicate a drier EM climate. In order to reconcile this dispute, workers have turned to marine and lacustrine sediment records.

Kolodny et al. (2005) use marine and terrestrial sediments to suggest that the long-term $\delta^{18}O$ trends observed in Soreq Cave speleothems are a result of changes in $\delta^{18}O$ of the Mediterranean Sea. Based on foraminiferal geochemistry, however, Almogi-Labin et al. (2009) argue that the $\delta^{18}O$ values observed in Soreq Cave cannot be explained solely by Mediterranean Sea surface $\delta^{18}O$, and that sea-land distance and relative elevation change due to lower sea levels must be accounted for as water vapor is transported from the EM to Soreq Cave.

Studies of pollen records near Soreq Cave (Baruch and Bottema, 1991, 1999; Bottema, 1995; Rossignol-Strick, 1995; Hajar et al., 2008; Langgut et al., 2011) show an increase in the abundance of temperate vegetation from the last glacial maximum (LGM) into the Holocene, indicating wetter climate in the Holocene. Rossignol-Strick (1995) concludes that oxygen isotope and pollen records from the EM and Arabian seas show two distinct climate regimes during the last deglaciation: a cold, arid Younger Dryas, and a temperate early Holocene with warm winters and wet summers.

The implication by Rossignol-Strick (1995) that seasonal climate differed between the Younger Dryas, the early Holocene, and the modern is a major motivation for the work presented here. Although some studies (Atkinson et al., 1987; Denton et al., 2005) have reported significant changes in Northern Hemisphere seasonality associated with millennial-scale warming (Bølling-Allerød) and cooling (Younger Dryas) events, few proxy records are capable of resolving seasonal climate across the Northern Hemisphere deglaciation. Denton et al. (2005) suggest that winter Arctic sea ice extended much further south in the Atlantic

during the Younger Dryas, resulting in relatively frigid winters but mild summers. Tierney et al. (2011) introduce the pairing of paleoclimate proxy data with an isotope-enabled climate model in order to identify seasonal climate changes as the cause for the East African Humid Period, 11-5 ka. The main goal of this study is to determine if Soreq Cave speleothems show the $\delta^{18}O$ signal of any significant seasonality changes during Northern Hemisphere deglaciation that can inform us about EM climate dynamics since the LGM.

Speleothem sample 2N preserves a record of calcite deposition across the last deglaciation. Although there are hiatuses in the growth record along the analytical traverse, we are able to interpret seasonality information from areas of consistent growth. The micro-imaging techniques used in this study allow us to recognize growth hiatuses, areas of irregular crystal growth, and non-calcite inclusions in a speleothem; we can then target ion microprobe analyses accordingly. Hence, this study utilizes the unparalleled spatial resolution of micro-analytical methodology to: (1) examine seasonality data over long time spans, and (2) reconstruct hemisphere-scale climate events that took place over short time spans. Prior studies from Soreq Cave, described in the following section, are integral to our climate interpretations.

1.3. Prior work at Soreq Cave

This investigation builds on prior characterization of Soreq Cave hydrology (Ayalon et al., 1998, 2004), the conventionally sampled 185 ka record of $\delta^{18}O$ from Soreq Cave speleothems (Bar-Matthews et al., 2003; Almogi-Labin et al., 2009), and analyses of both fluid inclusions (McGarry et al., 2004) and mass-47 CO_2 isotopologue anomalies (Δ_{47}) in Soreq speleothem calcite (Affek et al., 2008). These studies make Soreq an ideal natural laboratory to apply new procedures for high-precision analysis of $\delta^{18}O$ in 10 μm spots by ion microprobe and imaging of annual growth bands by confocal laser fluorescence microscopy (CLFM). Orland et al. (2009) developed the high-resolution methodology as part of a detailed study of $\delta^{18}O$ in a Soreq Cave stalagmite that grew from 2.2 to 0.9 ka. This study applies the high-resolution methodology to a stalactite that formed between 33.8 and 4.4 ka.

The geological and hydrological setting of Soreq Cave, located in the Judean Hills 20 km west of Jerusalem, is well described by numerous studies of Soreq speleothems and hydrology (Bar-Matthews et al., 1996, 1997, 2003; Ayalon et al., 1998, 1999, 2004; Matthews et al., 2000; Kolodny et al., 2003; McGarry et al., 2004; Orland et al., 2009; Bar-Matthews and Ayalon, 2011). In the modern EM, ~95% of the annual rainfall occurs during the winter "wet season," which extends from November until April. Over the past 15 years, average annual rainfall above the cave is ~500 mm. Furthermore, modern precipitation demonstrates an "amount effect," a negative linear correlation of the amount and $\delta^{18}O$ value of annual rainfall (Ayalon et al., 1998, 2004; Orland et al., 2009).

Critical for this study is the work of Ayalon et al. (1998, 2004) to examine rainfall and dripwater $\delta^{18}O$ values in and above Soreq Cave on a sub-annual timescale. They find that rainfall $\delta^{18}O$ values vary seasonally above Soreq Cave, with the lowest $\delta^{18}O$ values occurring during the peak of the winter wet season. Furthermore, Ayalon et al. (1998) and Orland et al. (2009) show that the modern pattern of seasonal $\delta^{18}O$ variability in rainfall is transmitted to dripwaters in the cave. We assume that seasonal $\delta^{18}O$ variability in paleorainfall was likewise transmitted to dripwaters. Next, we assert that the seasonal dripwater $\delta^{18}O$ signal is reliably recorded in Soreq speleothems.

Prior work in Soreq Cave indicates that it is reasonable to assume that $\delta^{18}O$ values in sample 2N reflect isotopic equilibrium with dripwater. Although Affek et al. (2008) find evidence for kinetic isotope effects in their measurements of Δ_{47} in Soreq Cave speleothems, they determine the corresponding effect on $\delta^{18}O$ to be negligible and ultimately conclude that their samples precipitated at near-equilibrium conditions for $\delta^{18}O$. Moreover, Bar-Matthews et al. (1996, 1997) established that sample 2N both passes the Hendy test for equilibrium precipitation (Hendy, 1971) and replicates the $\delta^{18}O$ variability of other samples from Soreq. Work in other caves (Mickler et al., 2006; Banner et al., 2007; Baldini et al., 2008) highlights the potential influence of seasonal pCO_2variability in a cave atmosphere on both isotopic equilibrium and seasonal growth rates. Since Soreq Cave had no natural entrance before it was discovered during a quarrying operation in 1968, seasonal ventilation of the cave atmosphere is presumed to have been insignificant. Additionally, Orland et al. (2009) demonstrate that the spatial resolution of our micro-analytical technique will allow us to account for changes in seasonal growth rates and avoid seasonally biasing the $\delta^{18}O$ record in sample 2N. Given these observations, we suggest that sample 2N precipitated in isotopic equilibrium and the $\delta^{18}O$ measurements we present here faithfully record a seasonal paleorainfall signal.

Orland et al. (2009) established guidelines to interpret combined $\delta^{18}O$ and CLFM data from the analysis of a late Holocene Soreq Cave calcite stalagmite (sample 2-6). CLFM imaging along the analytical traverse from the Holocene sample reveals a consistent sawtooth pattern of fluorescence intensity across concentric growth bands. The beginning of each growth band is marked by a sharp onset of bright-fluorescent calcite ("bright calcite"), followed by a gradual reduction in fluorescence intensity to dark-fluorescent calcite ("dark calcite") (Fig. 2A). The end of each growth band is marked by the sharp change to bright calcite in the next band. Ion microprobe analysis of the same analytical traverse shows that $\delta^{18}O$ values vary in a similar sawtooth pattern; the lowest $\delta^{18}O$ values occur at the sharp onset of bright calcite and then gradually increase as fluorescence gradually decreases.

Orland et al. (2009) interpret that these cycles represent annual banding and attribute the covarying patterns of fluorescence and $\delta^{18}O$ to a strongly seasonal rainfall pattern similar to the modern EM rainfall regime. They suggest that the onset of intense, low-$\delta^{18}O$ precipitation in the wet season flushes organic acids that accumulate in the upper soil column during the dry summer into the cave, causing the sharp onset of bright fluorescent, low-$\delta^{18}O$

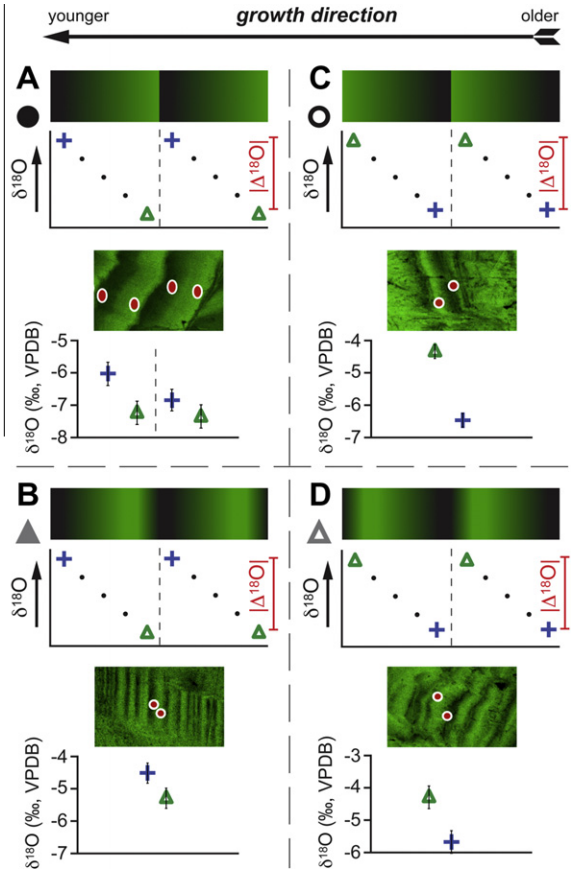

Fig. 2. Four patterns (A–D) of fluorescence and $\delta^{18}O$ variability within annual growth bands; each pattern is assigned a symbol for use in Figs. 3B and 5. A schematic illustration of each pattern is shown above an example from sample 2N. In each plot of $\delta^{18}O$, blue crosses and green triangles represent dark and bright fluorescent calcite, respectively. Error bars indicate 2 s.d. of each actual $\delta^{18}O$ analysis. Red spots in CLFM images show the location of ion microprobe analyses (~10 μm diameter). Note the definition of $|\Delta^{18}O|$ illustrated by the vertical bars.

calcite. Fluorescence intensity decreases and $\delta^{18}O$ values increase in the speleothem following the wet season flush, and the cycle repeats itself at the beginning of the following wet season.

In order to quantify seasonality, Orland et al. (2009) defined the variable $\Delta^{18}O$. Within a single annual growth band, $\Delta^{18}O(\text{dark-bright}) = \delta^{18}O(\text{dark calcite}) - \delta^{18}O(\text{bright calcite})$ (Fig. 2A). In sample 2-6, higher values of $\Delta^{18}O$(dark-bright) indicate more rain during the wet season, and thus a wetter year, while lower $\Delta^{18}O$(dark-bright) values indicate generally dryer conditions. This proxy of seasonality relies on the assumption that the modern pattern of distinct wet and dry seasons is consistent with the climate regime of the last 2.2 ka. In support of this assumption, Orland et al. (2009) observed that $\delta^{18}O$ values in dark-fluorescent calcite are relatively constant compared to $\delta^{18}O$ values of bright calcite (see their Supplementary Material). Thus, dark calcite reflects dry season dripwater from a mixed vadose zone reservoir and provides a "baseline" $\delta^{18}O$ value that changes slowly on a decadal scale. Therefore, in sample 2-6, it is the $\delta^{18}O$ value of bright calcite that varies from year to year, creating differences in $\Delta^{18}O$(dark-bright). This model of fluorescence and $\delta^{18}O$ values previously established in sample 2-6 will be evaluated with data from the past 34 kyr in sample 2N.

2. MATERIALS AND METHODS

2.1. U–Th dating

New U–Th disequilibrium ages of sample 2N, a stalactite composed of low-magnesium calcite (Bar-Matthews et al., 2000), were acquired by multi-collector inductively coupled plasma mass spectrometer analysis at the Geological Survey of Israel. The analytical method is described in Bar-Matthews et al. (2010). Twenty-four calcite aliquots were collected along a radial traverse of a 1 cm-thick slab of the speleothem, sawed orthogonally to the vertical growth axis. Calculated ages range from 4.5 ± 0.2 ka to 31.0 ± 0.9, and are corrected for excess ^{232}Th. The assumed initial $^{230}Th/^{232}Th$ activity ratio is 1.69, established in the detailed isochron study of Soreq Cave speleothems by Kaufman et al. (1998).

We define an "age model" for sample 2N based on linear interpolation between 11 selected U–Th dates. Of the 24 total ages measured, this simplified age model excludes: five measurements that incorporated irregular calcite growth (see Section 4.1.1 for further discussion) and eight ages that were bracketed by adjacent spots with overlapping error bars. The electronic annex Fig. EA-1 illustrates the overlap between the linear interpolation age model and a more complex Bayesian age model (Scholz and Hoffman, 2011) that includes all 24 ages. Given the excellent agreement between model types as well as our focus on the comparison of extended time periods, we think the linear interpolation model is suitable. Linear extrapolation of observed growth rates to the core and outer rim indicate that the $\delta^{18}O$ analyses presented here span from 33.8 to 4.4 ka. Table 1 lists the measured isotope ratios, uncorrected and corrected U–Th disequilibrium ages of all 24 measurements.

2.2. Sample preparation

A second 1-cm thick slab of stalactite 2N was cut adjacent to the piece dated at the Geological Survey of Israel and sent to the University of Wisconsin-Madison (UW-Madison) for ion microprobe analysis. At UW-Madison this slab was cut along its longest radius (13.8 cm) into 13 ~1 cm^3 cubes using a thin-kerf jeweler's saw. Fig. 1 shows where the 13 cubes (A-I, M-P) were cut from the slab of sample 2N and indicates the "working traverse" (white dashes) along which ion microprobe analysis was completed. The 13 cubes were mounted in pairs in seven 1-inch-diameter epoxy rounds (Fig. 1, inset). In each epoxy mount, 3–4 grains of UWC-3 (calcite standard; $\delta^{18}O = 12.49‰$, VSMOW; Kozdon et al., 2009) and the working traverse were placed within ~5 mm of the center of each mount to prevent instrument bias during ion micro-

Table 1
U/Th age data from multi-collector inductively coupled plasma mass spectrometry analysis of sample 2N.

Sample name	Distance from edge (mm)	U conc. (ppm)	$^{234}U/^{238}U$	$^{230}Th/^{234}U$	$^{230}Th/^{232}Th$	Age (yr) uncorrected	Age (yr) corrected
2N-1	**4.6**	**0.4200 ± 0.0003**	**1.02401 ± 0.00120**	**0.04735 ± 0.00070**	**13.10 ± 0.20**	**5300 ± 300**	**4500 ± 200**
2N-3B	**13.7**	**0.3898 ± 0.0003**	**1.01753 ± 0.00113**	**0.05845 ± 0.00094**	**10.29 ± 0.17**	**6500 ± 200**	**5400 ± 300**
2N-4C	17.0	0.3785 ± 0.0003	1.01523 ± 0.00130	0.05800 ± 0.00074	11.63 ± 0.15	6500 ± 200	5500 ± 300
2N-5B	18.9	0.3687 ± 0.0004	1.01733 ± 0.00135	0.06283 ± 0.00081	12.21 ± 0.16	7100 ± 200	6000 ± 300
2N-6	23.1	0.3682 ± 0.0002	1.01920 ± 0.00131	0.06597 ± 0.00117	13.71 ± 0.24	7400 ± 300	6000 ± 400
2N-7+8	27.2	0.5841 ± 0.0004	1.01891 ± 0.00120	0.05557 ± 0.00062	19.81 ± 0.22	600 ± 140	5600 ± 200
2N-11	36.3	0.3516 ± 0.0002	1.01923 ± 0.00152	0.06140 ± 0.00068	10.44 ± 0.12	6900 ± 180	5700 ± 300
2N-12	**40.8**	**0.3536 ± 0.0004**	**1.04713 ± 0.00150**	**0.08501 ± 0.00121**	**5.05 ± 0.08**	**9700 ± 280**	**6300 ± 400**
2N-13	**45.3**	**0.3219 ± 0.0002**	**1.03091 ± 0.00070**	**0.11127 ± 0.00094**	**6.05 ± 0.05**	**12900 ± 260**	**9200 ± 400**
2N-15	65.7	0.3757 ± 0.0002	1.05584 ± 0.00184	0.11004 ± 0.00129	7.01 ± 0.08	12700 ± 300	9600 ± 400
2N-16	**73.9**	**0.3898 ± 0.0003**	**1.03186 ± 0.00124**	**0.10284 ± 0.00074**	**16.40 ± 0.12**	**11800 ± 180**	**10600 ± 300**
2N-16+17	75.7	0.4195 ± 0.0002	1.03399 ± 0.00092	0.09253 ± 0.00062	19.65 ± 0.13	10600 ± 150	9600 ± 300
2N-17	77.6	0.3898 ± 0.0003	1.03454 ± 0.00136	0.14110 ± 0.00167	4.77 ± 0.06	16500 ± 420	10600 ± 500
2N-17B	**82.7**	**0.3611 ± 0.0004**	**1.02960 ± 0.00124**	**0.15299 ± 0.00172**	**4.40 ± 0.05**	**18000 ± 470**	**11200 ± 600**
2N-18	**88.2**	**0.3826 ± 0.0003**	**1.04747 ± 0.00163**	**0.14812 ± 0.00164**	**6.41 ± 0.07**	**17400 ± 500**	**12900 ± 500**
2N-20*	97.1	0.5672 ± 0.0004	1.05566 ± 0.00129	0.14313 ± 0.00123	18.46 ± 0.16	16800 ± 300	15300 ± 400
2N-20+21*	99.8	0.6384 ± 0.0007	1.05845 ± 0.00208	0.17045 ± 0.00184	7.50 ± 0.08	20300 ± 480	15800 ± 600
2N-21	**103.9**	**0.7739 ± 0.0006**	**1.05889 ± 0.00111**	**0.14585 ± 0.00094**	**27.70 ± 0.19**	**17100 ± 240**	**16100 ± 400**
2N-22*	108.5	0.5413 ± 0.0003	1.05795 ± 0.00107	0.20533 ± 0.00115	4.29 ± 0.03	24900 ± 350	15400 ± 600
2N-23*	113.9	0.3824 ± 0.0002	1.07316 ± 0.00118	0.20665 ± 0.00109	5.95 ± 0.03	21000 ± 300	18200 ± 400
2N-24*	121.3	0.4034 ± 0.0003	1.07005 ± 0.00199	0.18878 ± 0.00104	7.45 ± 0.04	22700 ± 300	17700 ± 400
2N-25	**124.7**	**0.5966 ± 0.0005**	**1.07111 ± 0.00147**	**0.19409 ± 0.00217**	**41.63 ± 0.49**	**23400 ± 600**	**22500 ± 700**
2N-26	**127.4**	**0.6305 ± 0.0004**	**1.06448 ± 0.00114**	**0.24987 ± 0.00330**	**17.45 ± 0.24**	**31200 ± 1000**	**28400 ± 1100**
2N-27	**129.8**	**0.5113 ± 0.0005**	**1.06262 ± 0.00089**	**0.25501 ± 0.00291**	**53.26 ± 0.67**	**32000 ± 840**	**31000 ± 1000**

All errors are listed at the 2σ confidence level. Ages used in the age model are in bold (see text for explanation, also Fig. EA-1). Ages from areas of irregular crystal growth are asterisked. The positions of age analyses in sample 2N are indicated in Fig. EA-4.

probe analysis related to sample position (Valley and Kita, 2005, 2009; Treble et al., 2007; Kita et al., 2009). Each round was polished using diamond paste in a progression from 6 to 1 μm grits and a final polish was applied using a colloidal alumina (0.05 μm) solution. Warm tap water and a soft toothbrush were used to remove any colloidal alumina residue. The polishing method was previously verified with sample 2-6 when imaging by reflected light profilometer confirmed a surface relief of less than 3 μm in the analytical portion of three epoxy rounds.

2.3. Confocal laser fluorescent microscopy

Imaging of the fluorescent growth bands in sample 2N was performed in the Keck Bioimaging Lab at UW-Madison with a Bio-Rad MRC-1024 scanning confocal microscope. A 40 mW laser with a wavelength of 488 nm coupled with an emission filter, which allows the transmission of fluorescent light with wavelengths between 505 and 539 nm, produced images of green growth bands. As we are unaware of a suitable method for fluorescence standardization, the focal plane depth, laser power, and signal gain were held constant in order to normalize image intensity. A series of 10–14 overlapping images (959 × 1199 μm) were collected with a 10× objective lens (100× total magnification) along the working traverse of each 1 cm-long sample chip. Stitched together, the fluorescence images – combined with reflected light image maps from an optical microscope – were used to select domains for ion microprobe $\delta^{18}O$ analyses.

2.4. Ion microprobe analysis of $\delta^{18}O$

High spatial resolution analyses of oxygen isotope ratios were completed on the CAMECA ims-1280 large radius multicollector ion microprobe at UW-Madison. Before insertion in the ion microprobe, each polished epoxy round was: (1) cleaned in a sonicator with both distilled water and ethanol; (2) gold coated with a coating thickness of ~60 nm; and (3) imaged with a reflected-light microscope for mapping purposes. The $\delta^{18}O$ analysis spots are oval with an approximate length of 10 μm in the long dimension; the sample was oriented so that the shorter dimension of the analysis spots was parallel to the working traverse. Using the standard-sample-standard bracketing technique outlined by prior workers (Kita et al., 2009; Kozdon et al., 2009; Orland et al., 2009; Valley and Kita, 2009), each block of sample analyses is assigned the precision of the bracketing standards. Thus, the spot-to-spot reproducibility of the 8 standard analyses bracketing each block of 10–15 sample analyses is assigned as the precision for those analyses. The average precision for the $\delta^{18}O$ spots on sample 2N is ±0.30‰ (2 standard deviations, s.d.).

Each $\delta^{18}O$ analysis spot is sputtered with a ~1.7 nA primary beam of $^{133}Cs^+$ ions, focused to ~10 μm diameter at the sample surface. Over the course of each 4 min analysis,

the beam ablates a ~1 μm deep pit in the calcite (~2 ng). Both the gold coating applied to the sample surface as well as a normal-incidence electron flood gun provide charge compensation. The secondary ion intensity for $^{16}O^-$ was generally 2.5×10^9 cps, depending on the primary beam intensity. The mass resolving power for the measurement of $\delta^{18}O$ is 2200; $^{16}O^-$ and $^{18}O^-$ ions are counted simultaneously on two Faraday cup collectors in multicollection mode. Further discussion of WiscSIMS analytical methods is presented elsewhere (Kita et al., 2009; Orland et al., 2009; Valley and Kita, 2009; Kozdon et al., 2011). Data are reported in Table EA-2.

The first analytical pass along the working traverse of each sample cube includes widely-spaced analyses that help define the general pattern of $\delta^{18}O$ variability across each sample section and to explore areas of interest. A more detailed analytical pass followed, with paired $\delta^{18}O$ analyses in the brightest and darkest fluorescent portion of 165 bands. Domains with visible surface pitting were avoided, except as discussed below. In the growth bands with paired analyses, analysis spots were placed in the widest, clearest portion of the fluorescent banding pattern.

After ion microprobe analysis, the gold coating was removed from each sample mount by lightly abrading the surface using a medium-nap pad wetted with 0.25 μm diamond suspension. Each sample mount was then reimaged by CLFM to classify the fluorescence (dark, bright, intermediate or mixed) of each analysis spot.

2.5. Post ion microprobe investigation

Following ion microprobe analysis, secondary electron and backscatter electron imaging by scanning electron microscopy was used to examine representative spots measured by ion microprobe. For analysis spots with imperfect pit-bottoms (e.g., cracks in calcite, microporosity) we used the respective ion yield values to check analytical validity. Analyses that are unimpeded by excessive porosity, irregular surface conditions, inclusions of other minerals, or primary beam aberrations have an expected range of ion yield values. As discussed below, we defined this range statistically for sample 2N and use it as the final test of validity for each spot.

A standard-sample-standard bracketing technique was used to determine the "percent yield" of each analysis relative to the average yield of the bracketing standards (Table EA-2). On average, analysis spots in sample 2N had yields that were 96.7% of the bracketing standard analyses. The Tukey definition of a suspected outlier (Tukey, 1977) limits the accepted range of "percent yield" values to between 93.2% and 100.4%. The 73 suspected outliers (<6% of 1223 sample analyses, highlighted in Table EA-2) are omitted from the plots and interpretations presented here.

As discussed further in Section 3.2, microporosity exists in some portions of sample 2N. Although some ion yield values from the most porous areas are classified as outliers by the Tukey definition, most fall within the accepted range and are included in the interpretations below.

3. RESULTS

3.1. CLFM imaging

CLFM reveals concentric fluorescent bands across the majority of the ~13 cm working traverse of sample 2N. Fluorescent bands are only absent in portions of the sample with "irregular crystal growth," discussed below. Each fluorescent band is defined by a single gradational transition between bright fluorescent calcite ("bright calcite") and dark, non-fluorescent calcite ("dark calcite"). Band widths vary from ~2 μm (2 pixels resolved by digital CLFM images) to 100 μm. Smaller bands may be common, but are not resolved by this technique.

Qualitative observation of the fluorescent banding across the working traverse of sample 2N reveals that there is significant variability in the banding pattern that is not seen in younger samples from Soreq cave (Fig. EA-3). Fig. 2 illustrates, in cartoon form, the four types of fluorescent banding pattern observed across the working traverse of 2N. From 10.5 ka to present in speleothem 2N, the fluorescence banding pattern is similar to that observed (Fig. 2A) throughout Holocene sample 2-6 (Orland et al., 2009). Specifically, each band has an abrupt onset of bright calcite followed by a gradient to dark calcite through time; the pattern repeats itself with an abrupt return to bright calcite at the beginning of the next band. Normal to the axis of elongation, the growth bands are concentric and crenulated; the growth fronts have a regular, chevron pattern. The chevron pattern reflects the radial c-axis orientation of calcite rhombohedra that precipitated on the outer surface of the stalactite. Linear truncations of the chevron pattern by a sharp fluorescent band, which occur in several intervals with irregular periodicity throughout sample 2N, are interpreted to represent dissolution of the outer surface of sample 2N and a time hiatus (see Fig. 5A in Orland et al., 2009).

Markedly different fluorescent banding patterns exist, however, in growth prior to 10.5 ka. From ~13.5 to 11 ka, the abrupt onset of fluorescence at the beginning of each band is commonly smoothed so that the majority of bands have a gradual gradient from bright to dark calcite as well as from dark to bright in the subsequent fluorescent band (Fig. 2B). This sinusoidal fluorescence intensity describes the majority of bands during this period.

Before 15 ka sinusoidal fluorescence is also common, but the fluorescence pattern observed within some annual bands is reversed with respect to Holocene growth described above. As a result, two more banding categories are observed. A number of the annual growth bands during this time period have a reversed sawtooth fluorescence pattern (Fig. 2C). Rather than the bright-to-dark progression of Holocene bands, a sharp dark boundary indicates the beginning of these bands. A gradient to bright fluorescence then lasts until the end of the band, where the next sharp dark boundary occurs. The fourth banding category (Fig. 2D) is identical in fluorescence pattern to the gradational transitions in Fig. 2B, but ion microprobe analysis indicates that the oxygen isotope gradient is reversed as discussed below. All four of the fluorescence patterns described above are present before 22 ka.

These banding pattern classifications are first made by visual examination of the CLFM images and then interrogated by ion microprobe analysis of $\delta^{18}O$. The difference between the banding patterns described in Figs. 2B and 2D is determined by whether the bright calcite has a lower $\delta^{18}O$ value than the adjacent dark calcite (2B) or vice versa (2D).

There are three areas of the working traverse where calcite crystals have an irregular habit and do not contain concentric fluorescent bands (arrows in Fig. 1). There are no calculated values of $\Delta^{18}O$ in these areas. This irregular calcite is identified by CLFM and indicated as "irregular crystal growth" in Fig. 3A (hashed vertical rectangles), calcite crystals form a cross-hatched pattern with a much higher porosity relative to the rest of the sample. The irregular crystal growth, discernable to the naked eye on a polished surface, is clearly identified in both reflected-light (Fig. 1) and CLFM imaging (Fig. EA-3). Further discussion of this material is in Section 4.1.1.

3.2. Ion microprobe analysis of $\delta^{18}O$

Results of the 1223 $\delta^{18}O$ sample analyses and 589 standard measurements are recorded in chronological order of analysis in Table EA-2. The $\delta^{18}O$ values measured in sample 2N range from −9.1‰ to −2.5‰ (VPDB). Figure EA-4 plots the $\delta^{18}O$ value and the fluorescence classification of each ion microprobe spot. In Fig. 3A, which shows analyses with either dark or bright fluorescence classifications, an 11-point running average is plotted for only dark calcite spots between 14 and 0 ka. The running average illustrates the high $\delta^{18}O$ "baseline" of this dataset since 14 ka.

Imaging of ion microprobe pits by backscatter electron imaging reveals that some dark fluorescent calcite in older portions of sample 2N contains microporosity (Fig. EA-5). Void spaces in the microporous regions tend to have elongated shapes with long axes parallel to the radial growth direction of calcite crystals. Inspection of backscatter electron images from areas with microporosity indicates that most void spaces have a maximum dimension less than 1 μm in length, do not appear to be interconnected, and amount to at most ~7% of the total area in a single pit-bottom. To ensure that the microporosity, which varied in its distribution along single bands, did not affect ion microprobe analyses, we made a total of 63 $\delta^{18}O$ measurements along seven 0.5–2 mm traverses parallel to bands displaying microporosity (Table EA-6). The mean value of two standard deviations of the seven groups of $\delta^{18}O$ analyses along individual bands is 0.71‰, approximately two times the average spot-to-spot precision (2 s.d.) of the bracketing UWC-3 calcite standard analyses obtained during these analyses (0.31‰).

Some excess in variability of the along-band analyses as compared to standard analyses is expected. Orland et al. (2009) showed that $\delta^{18}O$ within annual growth bands is zoned, thus, slight variability in the positions of analysis spots along the strike of an annual band results in greater heterogeneity than the homogeneous calcite standard. Furthermore, the greatest intra-band $\delta^{18}O$ variability is ob-

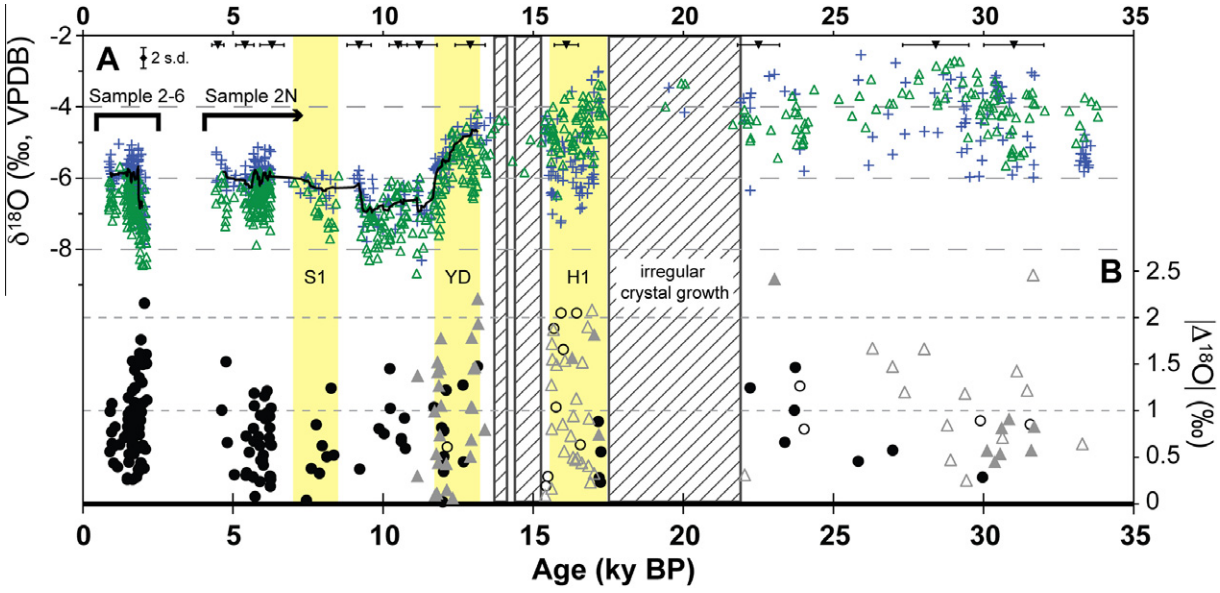

Fig. 3. (A) shows the measured $\delta^{18}O$ (‰, VPDB) values for ion microprobe analysis of the brightest (green triangles) and darkest (blue crosses) fluorescent calcite within each band across sample 2N (34–4 ka). Data from sample 2-6 (Orland et al., 2009) is included from 2.2 to 0.9 ka to illustrate the continuity of $\delta^{18}O$ and fluorescence patterns in different samples during the Holocene. During the Holocene, higher $\delta^{18}O$ values represent drier climates while lower $\delta^{18}O$ values are characteristic of wetter climates. The heavy black line, an 11-point running average of dark calcite from ~14-4 ka, shows the general trend of "baseline" $\delta^{18}O$ values during periods of time when dark calcite has consistently higher $\delta^{18}O$ values. Zones of irregular calcite growth are outlined by the hashed rectangles between 22 and 14 ka. U–Th ages with 2σ errors and the average 2 s.d. for $\delta^{18}O$ measurements (0.30‰) are shown at the top. Panel (B) shows values of $|\Delta^{18}O|$ [where $\Delta^{18}O = \delta^{18}O(\text{dark calcite}) - \delta^{18}O(\text{bright calcite})$] of individual bands. See Fig. 2 for the explanation of the symbols used to plot $|\Delta^{18}O|$. The Younger Dryas (YD), Heinrich 1 (H1), and Sapropel 1 (S1) events are highlighted with yellow shaded bars. Dates for H1 are from Bard et al. (2000), and dates for S1 are from Bar-Matthews et al. (2000).

served along bands that have the highest degree of microporosity in sample 2N (as inferred from optical microscopy and anomalously low ion yield values). These are bands that would otherwise be avoided by the analyst. Thus, we are confident in measurements of $\delta^{18}O$ within bands that display lesser degrees of microporosity.

3.3. Calculating $\Delta^{18}O$(dark-bright)

Orland et al. (2009) proposed that the difference in $\delta^{18}O$ values between the bright and dark fluorescent calcite of a single annual band [$\Delta^{18}O(\text{dark-bright}) = \delta^{18}O(\text{dark}) - \delta^{18}O(\text{bright})$] represents a quantitative measure of seasonality. While all values of $\Delta^{18}O$(dark-bright) are positive in sample 2-6, fluorescent banding patterns are occasionally reversed (i.e., dark-to-bright, Figs. 2C and D) in sample 2N such that $\Delta^{18}O$(dark-bright) values are negative in 52 (32%) of the 165 analyzed bands. Where the fluorescent banding pattern is reversed, $\delta^{18}O$ values in bright calcite are higher than $\delta^{18}O$ values in dark calcite. Note, however, that the sawtooth pattern of $\delta^{18}O$ variability remains the same across each band, irrespective of fluorescence; lower $\delta^{18}O$ values always precede higher $\delta^{18}O$ values.

We simplify visual comparison of $\Delta^{18}O$ across sample 2N by plotting $|\Delta^{18}O|$(dark-bright), the magnitude of the $\delta^{18}O$ gradient within single annual bands, in Fig. 3B. Fig. 2 illustrates how $|\Delta^{18}O|$ values are calculated from different fluorescent banding patterns. The calculated values of $|\Delta^{18}O|$ range from 0.0‰ to 2.5‰. No relationship is evident between $|\Delta^{18}O|$ values and band widths.

4. DISCUSSION

Coupled changes in $|\Delta^{18}O|$ and fluorescent banding in sample 2N indicate multiple significant environmental changes above Soreq Cave in the last 34 kyr. Given the complexities of the ocean-atmosphere-soil-cave system and the lack of similar seasonal records in the literature, the interpretations we outline below are ripe for further interrogation. We examine the results from the perspective of, first, only the fluorescent banding data, and second, after incorporating the oxygen isotope data.

4.1. Interpretation of fluorescent banding

The occurrence of fluorescence at the excitation and emission wavelengths used in CLFM imaging of sample 2N indicates that the fluorescent bands we observe are likely a result of seasonal variability of organic acids in cave dripwaters (Senesi et al., 1991; Baker et al., 1996; McGarry and Baker, 2000; Tan et al., 2006). The combination of the hydrologic setting of Soreq Cave with distinct seasonal rainfall further supports the idea that fluorescent banding in Soreq speleothems is caused by annually variable organic acid infiltration (Orland et al., 2009). For much of sample 2N, fluorescent bands are easily discernable and many have widths of 10–50 μm. Two features of the fluorescent banding are discussed in more detail below: (1) areas of irregular banding where calcite crystal growth is atypical, and (2) variability in the pattern of fluorescent banding (as in Fig. 2).

4.1.1. Irregular banding pattern

There are portions of sample 2N, highlighted by three hashed rectangles between 22 and 14 ka in Fig. 3A, where the crystal habit of speleothem calcite takes on an irregular, lattice-type structure (Figs. 1, EA-3). Fig. 1 shows that these domains are lenses that pinch out. Thus, while any continuous-growth age model would assign long periods to these zones, their growth duration is uncertain, especially before Heinrich event 1 (H1). There are three likely explanations for the irregular crystal growth habit. First, Bar-Matthews et al. (2003) find that speleothems with regular growth during these time periods have consistent isotopic profiles. Hence, the most likely explanation for the irregular crystal growth habit is a change in the local hydrologic character of the cave-groundwater system (i.e. drip supply) where sample 2N was growing.

Second, a change in environmental factors within the cave (i.e. cave humidity, pCO_2 of the cave atmosphere) may have resulted in a different physical or chemical mechanism of calcite precipitation. Interestingly, these irregular portions are coincident with periods of time, the LGM (~20 ka) and Bølling–Allerød (~14 ka), which other Northern Hemisphere proxies (McGarry et al., 2004; Affek et al., 2008; Almogi-Labin et al., 2009) identify as having vastly different environmental conditions: the LGM was cold and dry, while the Bølling–Allerød was warm and wet. Perhaps the resumption of concentric banding at the onset of Heinrich 1 (H1) and Younger Dryas (YD) climate events (Fig. 3) is a clue for the cause of banding variability.

Third, it is possible that the irregular crystals formed as a result of calcite recrystallization in the speleothem. U–Th ages determined from irregular calcite crystals are within error of the ages in adjacent, "regular" crystal growth, suggesting that if this material was recrystallized, either the U/Th ratio was preserved or calcite replacement happened soon after primary precipitation of the speleothem calcite. Furthermore, the irregular calcite does not cut across adjacent banding patterns, suggesting that it accumulated on the outer surface of the speleothem and was later covered by regular calcite growth. Since the cause of the irregular crystal growth may be a change in the local hydrological environment and/or regional climate, we avoid interpreting the $\delta^{18}O$ data analyzed in these zones. Notably, $\delta^{18}O$ values that were measured in the irregular calcite (included in Figs. 3, EA-4) do not change the interpretations that follow.

4.1.2. Fluorescent pattern variability

This section outlines hypothetical climatic interpretations of the fluorescent banding patterns that are characteristic of different portions of sample 2N (Fig. 2). Discussion in subsequent sections will include oxygen isotope data.

Throughout the portion of sample 2N that grew after 10.5 ka, annual growth bands are characterized by a sharp onset of bright fluorescence followed by a gradual return to dark fluorescence (Fig. 2A). Here we adopt the fluorescence-climate interpretation of Orland et al. (2009). Specifically, the onset of heavy rain events at the beginning of the winter wet season transports organic acids, which accumulated in the upper soil column during the dry season, into the cave where they are trapped in speleothem calcite.

Based on the consistency of speleothem fluorescent banding, we suggest that the modern, annual pattern of distinct wet and dry seasons was the dominant climate regime in the EM for at least the last 10.5 ka.

Before 10.5 ka, sample 2N records two additional patterns of fluorescent banding: fluorescence intensity that varies sinusoidally across bands (Figs. 2B and D) and dark-to-bright fluorescence patterns (Figs. 2C and D) that are reversed relative to the bright-to-dark Holocene pattern. Gradual sinusoidal transitions between bright and dark calcite suggest that rainfall was more consistent during the onset and termination of organic acid production in the soil, perhaps due to a reduced gradient in seasonal rainfall or a change in organic acid production. During the YD, when pollen records (Rossignol-Strick, 1995; Langgut et al., 2011) indicate that semi-arid species dominate EM vegetation, a different plant population may have caused distinct fluorescent patterns by altering the timing, type or amount of organic acid delivery into the cave.

The reversed fluorescence patterns suggest multiple possible changes in the manner that organic acids are delivered into Soreq Cave. We present four potential explanations for the intermittent reversals in the order of fluorescence banding before 15 ka. (1) A change in the timing or rate of organic acid production in the soil column relative to wet season rainfall events. (2) Reduced seasonality of rainfall (i.e. less distinct wet and dry seasons). (3) Snowfall or frozen ground during the winters of H1 and YD. (4) A change in the dominant type or amount of vegetation. Hypotheses for both reversed and sinusoidal fluorescence patterns are evaluated in the following section by considering $\delta^{18}O$ and $\Delta^{18}O$ values within annual bands.

4.2. Interpretation of $\delta^{18}O$ and $\Delta^{18}O$ values

Almogi-Labin et al. (2009) examined conventionally measured $\delta^{18}O$ values in sample 2N and found that they agree with the (inverse) NGRIP Greenland ice core $\delta^{18}O$ record. Thus, the $\delta^{18}O$ data reported in Fig. 3A, which include all ion microprobe measurements in bright and dark fluorescent calcite from samples 2N and 2-6, are used to help guide the identification of the major climatic periods. Following the LGM, Fig. 3A illustrates that $\delta^{18}O$ values record: (1) the end of the LGM, H1; (2) the onset, duration, and termination of the YD; and (3) the Holocene up to ~0.9 ka.

By themselves, $\delta^{18}O$ values from the late Holocene can be used to interpret a regional history of seasonal climate based on the modern "amount effect". But what about before the Holocene, when the climate modes in the North Atlantic and EM were significantly different? Can we apply the present-day amount effect as suggested by Bar-Matthews et al. (2003)? Recent studies suggest caution (Vaks et al., 2006; Almogi-Labin et al., 2009). They note that lower sea levels during the LGM effectively moved Soreq Cave inland and to a higher elevation relative to its Holocene position. This would increase Rayleigh fractionation of water vapor during transport to the cave and decrease local rainfall $\delta^{18}O$ values by ~1–1.5‰ during the LGM, independent of rainfall amount (Vaks et al., 2006; Almogi-Labin et al., 2009).

The advantage of the micro-analytical approach presented here is that we are able to consider two features in addition to $\delta^{18}O$ values: the fluorescent pattern of annual growth bands discussed above and calculated values of $|\Delta^{18}O|$(dark-bright). We consider all three factors in parallel for the climate interpretations below.

4.2.1. The Holocene

Orland et al. (2009) found that $\delta^{18}O$ and $\Delta^{18}O$(dark-bright) values could be used together to examine hydrological characteristics of Soreq Cave. A plot of $\delta^{18}O$ vs. $\Delta^{18}O$(dark-bright) using data from late Holocene sample 2-6 (Fig. 7 in Orland et al., 2009) illustrates that the $\delta^{18}O$ of dark calcite is relatively consistent while the $\delta^{18}O$ of bright calcite is more variable and, thus, dictates $\Delta^{18}O$ values. Orland et al. (2009) describe dark calcite as representing "baseline" dripwater that entered the cave from a vadose zone reservoir during the dry season and bright calcite reflects infiltration of wet-season precipitation. It is clear that the distinct wet/dry seasonal climate of the late Holocene is reflected in $\Delta^{18}O$ data.

For sample 2N, a similar plot of $\delta^{18}O$ vs. $|\Delta^{18}O|$(dark-bright) for analyses dated between 10.5 and 4 ka (Fig. 4) shows a nearly identical pattern to the late Holocene sample examined by Orland et al. (2009). Namely, the $\delta^{18}O$ values of dark calcite in 2N after 10.5 ka are relatively consistent, while the $\delta^{18}O$ values of bright calcite are more variable and dictate $|\Delta^{18}O|$ values. Thus, the isotope data confirm the fluorescent banding interpretation described above: the climate regime of distinct wet and dry seasons persists throughout the Holocene in the EM. This conclusion does not point to a persistence of wet summers in the early Holocene as proposed by Rossignol-Strick (1995).

We note two additional features of Holocene $\delta^{18}O$ and $|\Delta^{18}O|$ values. First, the running average of baseline (dark) $\delta^{18}O$ values increases ~1‰ from 10.5 to 5 ka (Fig. 3A). Lower $\delta^{18}O$ values in the early Holocene likely reflect contributions of meteoric water (low $\delta^{18}O$) from a combination

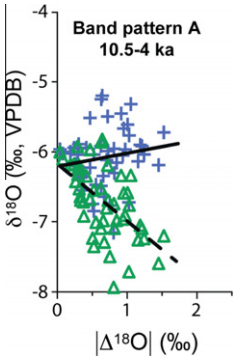

Fig. 4. Plot of $\delta^{18}O$(calcite) vs. $|\Delta^{18}O|$(dark-bright) for every pair of analyses within a single annual band between 10.5 and 4 ka ($n = 49$). As in Fig. 3, green triangles represent $\delta^{18}O$ measurements made in bright calcite and blue crosses represent $\delta^{18}O$ measurements made in dark calcite. Linear best-fit regressions of each population illustrate trends discussed in the text. The dashed line is fit to measurements in bright fluorescent calcite ($R^2 = 0.33$) and the solid line (mean = −6.08‰, s.d. = 0.42‰) is fit to measurements in dark calcite.

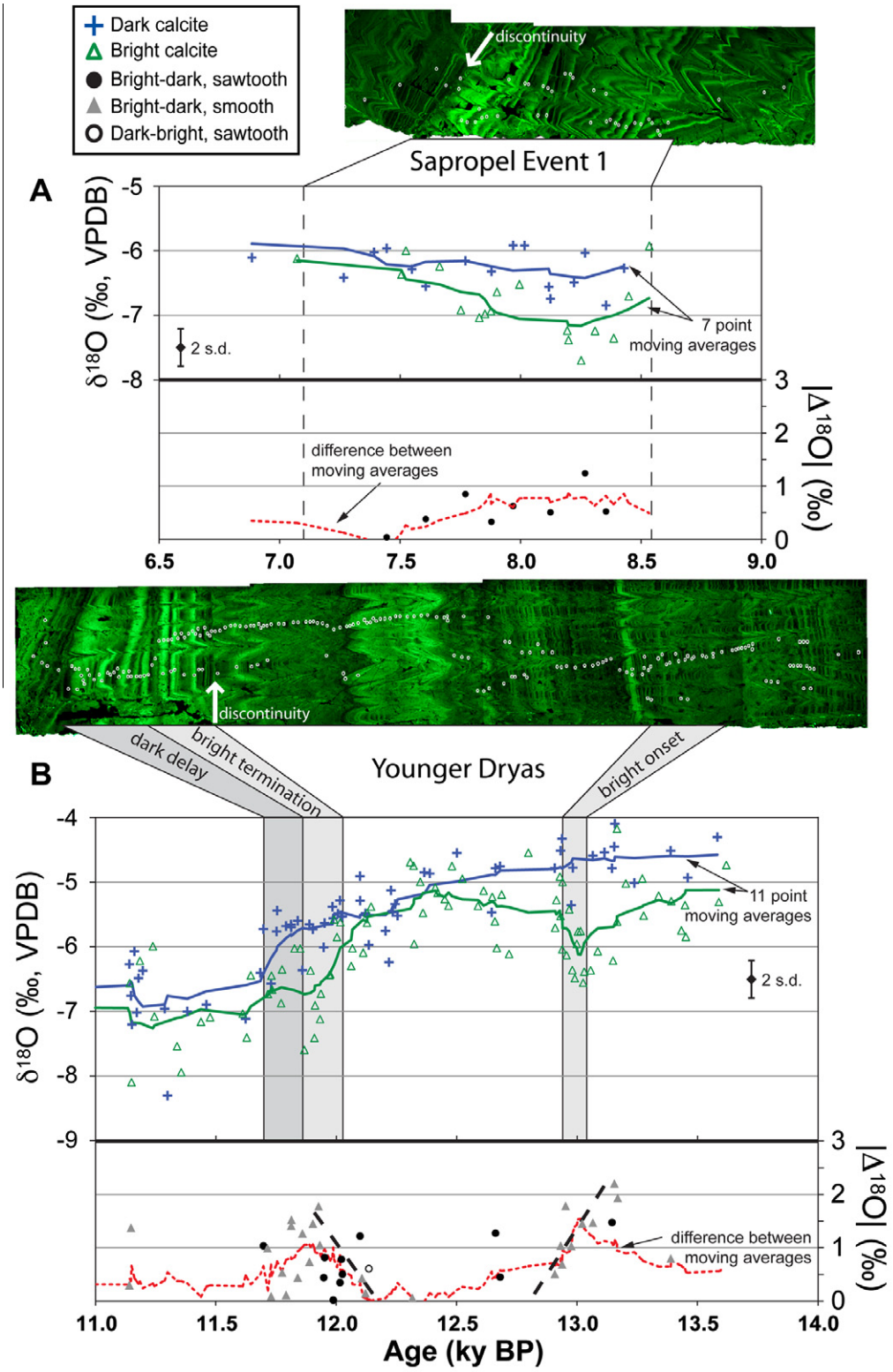

Fig. 5. Oxygen isotope data and CLFM imaging of sample 2N across the Sapropel 1 (panel A) and Younger Dryas (panel B) events. In both panels A and B, the upper portion of the graph shows $\delta^{18}O$(calcite) values across the climate event as recorded in sample 2N. The solid lines indicate running averages of the $\delta^{18}O$ data values with dark and bright fluorescent classifications. The lower portion of each graph plots $|\Delta^{18}O|$(dark-bright) across the same time period. The red dotted lines indicate the difference between the running averages of dark and bright $\delta^{18}O$ analyses. In panel B, the heavy dashed line illustrates an interesting pattern of $|\Delta^{18}O|$ variability at the onset and termination of the Younger Dryas (see text for discussion). The corresponding CLFM images from sample 2N are stitched together above the graphs and the shaded boxes indicate corresponding portions of the $\delta^{18}O$ record. The white arrows in the CLFM images show the location of banding discontinuities.

of enhanced westerlies that cause rainfall over the entire Mediterranean (Kallel et al., 1997) and increased freshwater runoff from the Nile into the EM as a result of the orbitally driven African Monsoon (Marino et al., 2008).

Second, there is an interesting isotopic change across Sapropel event 1 (S1, 8.5–7.0 ka; Bar-Matthews et al., 2000), which is identified in other Soreq speleothems (Bar-Matthews et al., 1999, 2000) and highlighted in Figs. 3 and 5A. S1 is defined stratigraphically by anoxic marine sediments that form as a result of Nile runoff and increased EM density stratification (Rossignol-Strick et al., 1982; De Lange et al., 2008). Hence, lower $\delta^{18}O$ values are expected in Soreq speleothems. Indeed, there is an excursion of $\delta^{18}O$ analyses in bright calcite to lower values, but $\delta^{18}O$ values of dark "baseline" calcite remain relatively unchanged. As a result, $|\Delta^{18}O|$ values are larger during S1 with a peak at 8.3 ka. Although the increase in $|\Delta^{18}O|$ values across this time period agrees with the interpretation that S1 is a wet period at Soreq (Bar-Matthews et al., 2000), it is curious that the dark baseline $\delta^{18}O$ values do not change. The consistent $\delta^{18}O$ values in dark domains suggest that either: (1) the residence time of baseline vadose groundwater is long enough that deluge events during S1 winters do not perturb $\delta^{18}O$ values of summer dripwater; (2) Rayleigh distillation increases the $\delta^{18}O$ of summer rainfall to balance the $\delta^{18}O$ decrease of EM source water; (3) the $\delta^{18}O$ value of source water did not decrease significantly due to freshwater input from the Nile; or (4) sample 2N does not fully record S1. The number and length of growth hiatuses in this section of the sample are unknown; although the pattern of $\delta^{18}O$ values across this section of the speleothem may be representative of the entire S1 event, it is possible that sample 2N only records a portion of the S1 event. We can pin the location of S1 in sample 2N if future ion probe analysis of $\delta^{13}C$ identifies the large, positive $\delta^{13}C$ excursion that is reported in other Soreq speleothems (Bar-Matthews et al., 2000).

4.2.2. The Younger Dryas

Prior to 10.5 ka, both the fluorescent banding patterns and $|\Delta^{18}O|$ values in sample 2N are consistently different than in the Holocene. Qualitative observation of CLFM imaging from the YD, the duration of which is inferred from $\delta^{18}O$ values shown in Fig. 5B, indicates that the majority of bands have sinusoidal fluorescence intensity. Notably, the scarcity of measurable $|\Delta^{18}O|$ values from the height of the YD is due to narrow banding; reliable paired analyses of $\delta^{18}O$ within individual bands during the YD are rare in sample 2N. The onset and termination of the YD event are characterized in sample 2N with wider fluorescent banding, and thus, reliable $|\Delta^{18}O|$ analyses.

The onset of the YD is marked by a decrease in $|\Delta^{18}O|$ values (Fig. 5B). Although there are few $|\Delta^{18}O|$ measurements from the height of the YD, the convergence of the running averages of bright and dark $\delta^{18}O$ analyses (dotted line, Fig. 5B) suggests $|\Delta^{18}O|$ is low during this period. In combination with the sinusoidal fluorescence pattern of the YD, the transition to low $|\Delta^{18}O|$ values may indicate a decrease in seasonality and reduced annual rainfall. Colder conditions year-round during the YD (Denton et al., 2005; Almogi-Labin et al., 2009) could reduce evaporation-induced fractionation of rainwater and shallow groundwater, thus lowering $|\Delta^{18}O|$. Furthermore, since cooler conditions would reduce organic decomposition rates in the soil (Davidson and Janssens, 2006) and widen the temporal window of organic acid production in the overlying soil, the sinusoidal fluorescent banding pattern is likely caused by a more consistent year-round supply of dripwater to the cave. While the narrow bands and reduced $|\Delta^{18}O|$ values in sample 2N point to lower annual rainfall totals during the YD, we cannot make a quantitative estimate of annual rainfall for this period.

The pollen records that were briefly discussed in the introduction indicate that YD vegetation in the EM is not only different from that in the Holocene, but also suggest a more arid regional climate. This agrees with our hypothetical explanation of YD seasonal climate and provides another potential cause for the sinusoidal fluorescent banding pattern. Perhaps decomposition of the herbaceous vegetation of the YD (Hajar et al., 2008) produces different types or amounts of organic acids in a different seasonal time window. For now, however, we prefer the reduced seasonality explanation for sinusoidal fluorescent banding since it better explains the combined fluorescence and isotopic results.

Fig. 5B illustrates that sample 2N records the YD termination in two stages. First, there is a period ("bright termination") where the $\delta^{18}O$ values of bright calcite decrease $\sim 2‰$ while dark calcite $\delta^{18}O$ is relatively unchanged. This first stage causes a steady increase in maximum $|\Delta^{18}O|$ values, mirroring the gradual decrease at the YD onset (see dashed line, Fig. 5B). In the second stage ("dark delay"), dark calcite $\delta^{18}O$ values remain high while bright calcite $\delta^{18}O$ values remain low. Near the end of the second stage, the $\delta^{18}O$ value of dark calcite abruptly reduces by $\sim 1.5‰$ so that both bright and dark calcite $\delta^{18}O$ have approached their approximate Holocene values. The delayed response of dark band $\delta^{18}O$ values fits with the interpretation of Soreq Cave hydrology (Orland et al., 2009). The integrated "baseline" $\delta^{18}O$ value of vadose groundwater is represented by dark calcite growth and lags the surface-driven signal recorded in bright calcite. We interpret that a combination of rapid reduction of EM surface water $\delta^{18}O$ values and increased seasonal rainfall drives the large drop in bright $\delta^{18}O$ values, and the residence time of the vadose zone prevents an immediate response of dark $\delta^{18}O$ values. It is unclear why a similar delay is not observed at the onset of the YD.

We highlight two further observations from the CLFM imaging in Fig. 5B: (1) the pattern of banding across the YD termination, and (2) the number of bands across the termination. Following the duration of the YD, where fluorescent bands are closely spaced with subtle fluorescence gradients, bands become wider and brighter at the termination. This suggests that the termination was a period of significant, rapid climatic change and that the coincident shift in $\delta^{18}O$ values does not just reflect a shift in the $\delta^{18}O$ value of the rainwater source (i.e., EM surface waters).

We estimate a minimum duration of the YD termination in the EM by counting the number of fluorescent bands

across the $\delta^{18}O$ gradients identified by ion microprobe analysis. Across the first stage, "bright termination", there are 12 fluorescent bright-dark couplets following an apparent discontinuity. Thus, at a minimum (assuming no hiatuses or years of little growth during this stage), the full passage of the YD termination as reflected in EM rainfall took place over 12 years. This time span is consistent with other climate proxies that constrain environmental responses to the YD termination to a decadal scale (Taylor et al., 1997; Severinghaus et al., 1998; Steffensen et al., 2008). Across the second stage, "dark delay", there are 10 more fluorescent bright-dark couplets that represent the extra time required to complete the isotopic shift in dripwaters that reached sample 2N.

4.2.3. Heinrich event 1 and last glacial period

Prior to 15 ka, $\Delta^{18}O$ values are different from those in the Holocene and YD in two important ways: first, the mean of $|\Delta^{18}O|$ values is higher, and second, "reversal" of the fluorescent banding pattern is common and results in negative values of $\Delta^{18}O$ (open circles and open triangles in Fig. 3B). These differences in $|\Delta^{18}O|$ and fluorescent banding must be due to environmental changes, which are hypothesized below.

Before 15 ka, the mean value of $|\Delta^{18}O|$ is 1.0 with a standard deviation of 0.6; after the YD event, the mean value of $|\Delta^{18}O|$ decreases to 0.7 with a standard deviation of 0.4. A student t-test suggests that we can reject the null hypothesis (that populations have equivalent mean values) with >99% confidence. Further, a Kolmogorov-Smirnov test indicates that the cumulative distributions of each population differ significantly, with >98% confidence.

One possible cause of higher mean $|\Delta^{18}O|$ values before 15 ka is a more intense seasonal rainfall gradient; wetter wet seasons (with lower $\delta^{18}O$ values) would cause larger $|\Delta^{18}O|$ values. Similarly, a pulse of spring meltwater in periods with winter snowfall would introduce lower $\delta^{18}O$ values to the cave, resulting in increased $|\Delta^{18}O|$ values. Consider another scenario however, where rainfall persists year-round and there is no discernable dry season or baseline dripwater $\delta^{18}O$ value. Increased rainfall during warm months, when $\delta^{18}O$(rain) is higher than in winter months, would cause a wider annual range of dripwater $\delta^{18}O$ and thus, larger $|\Delta^{18}O|$ values. Therefore, in order to identify the most likely climatic interpretation of higher $|\Delta^{18}O|$ values, we must consider the reversal in fluorescent banding pattern.

Here, we examine four hypothetical environmental causes for the "reversed" fluorescent banding patterns (Figs. 2C, 2D) before 15 ka. (1) A change in the relative timing of the wet season and the production of organic acids above the cave might cause the organic acids to appear in a different location in the growth band. (2) A reduced gradient of annual rainfall amount (i.e. less distinct wet and dry seasons) could change the timing of organic acid delivery into the cave. (3) Snowfall during H1 and YD winters might delay delivery of organic-poor dripwaters each year until spring melt, causing a sharp onset of dark calcite. (4) A change in the dominant type or amount of vegetation could alter the type and timing of organic acid production and the resultant fluorescent banding.

The first suggestion (hypothesis #1) is that given bimodal wet and dry seasons, a change in the timing of wet season rainfall events relative to the production of organic acids would change the pattern of fluorescence relative to the $\delta^{18}O$ value of calcite. Although such a scenario seems possible, it is unrealistic since the wet season determines the timing of the growing season. As long as low-$\delta^{18}O$ rainfall is coincident with wet seasons that flush accumulated organic acids into the cave, then low $\delta^{18}O$ calcite will have bright fluorescence.

The second suggestion (hypothesis #2) is that a reduced gradient of annual rainfall may contribute to the shift in the timing of fluorescence delivery relative to the observed $\delta^{18}O$ gradient. Even with lower annual rainfall totals than in the Holocene, it is conceivable that relatively consistent year-round rainfall would result in organic acids being delivered to the cave as they are produced rather than after accumulating during a dry season (as in the Holocene). Although year-round rainfall would probably not cause sharp fluorescent boundaries (as in Fig. 2C), such a scenario could result in the "reversed" sinusoidal pattern of fluorescence intensity illustrated in Fig. 2D. Furthermore, given consistent year-round rainfall, we would anticipate a plot of $\delta^{18}O$ vs. $\Delta^{18}O$ to show no evidence of the consistent baseline $\delta^{18}O$ values observed in Holocene growth (Fig. 4). Indeed, for "reversed sinusoidal" (Fig. 2D) bands between 34 and 15 ka there is not a consistent $\delta^{18}O$ baseline (Fig. EA-7D). Therefore, a reduced gradient of seasonal rainfall may cause the "reversed sinusoidal" bands. But what about the "reversed sawtooth" (Fig. 2C) bands, which exhibit a $\delta^{18}O$ baseline in bright calcite (Fig. EA-7C)?

If snow cover and frozen ground persisted through the winter above Soreq Cave (hypothesis #3) this would reduce or stop both water flow and organic decomposition above the cave during the season that presently has the highest drip rates and forms bright calcite. The melting of snow in spring would then contribute a large amount of low-$\delta^{18}O$ water to the cave. If late fall rains removed organic acids from overlying groundwaters, then the snowmelt would contain few organic acids. This scenario would account for the sharp onset of dark calcite. Bands with a sharp onset of dark fluorescence occur during the cold glacial period and H1 event, when snowfall was possible.

A change in vegetation (#4) is another hypothesized cause of the fluorescence reversal. Perhaps different plant species delivered a distinct suite of organics to the soil before 15 ka, or perhaps the same organics were delivered on an alternate schedule. At present, $\delta^{13}C$ values provide the only record of vegetation changes measured in Soreq speleothems; given the assumption of isotopic equilibrium in Soreq samples, there would be a notable signal in $\delta^{13}C$ values if a shift in the ratio of C3- and C4-type plants occurred. Conventional analyses of $\delta^{13}C$ in Soreq speleothems (Bar-Matthews et al., 1997) show that vegetation changes gradually from a mix of C3 and C4 plants during glacial periods to C3-dominated interglacial periods. This gradual change does not fit the discreet difference in banding patterns before and after 15 ka. If the plant population were to change abruptly without altering the C3/C4 ratio, however, isotopic data alone would not distinguish the shifting

ecosystem. Langgut et al. (2011) offer the most reliable regional pollen record across the deglaciation. Interestingly, they document a more rapid change to temperate vegetation than indicated by Soreq $\delta^{13}C$ measurements. Going forward, one way to resolve this discrepancy – albeit at low resolution – might be by direct analysis of lipid compounds in sample 2N (e.g., Rushdi et al., 2011).

It is evident that, independent of other regional paleoclimate records, the fluorescence reversal represents a regional climatic response. We suggest that "reversed sinusoidal" fluorescent bands (Fig. 2D) during H1 may indicate a year-round supply of dripwater to the upper soil column and cave. Furthermore, bands with "reversed sawtooth" fluorescence (Fig. 2C), most common during the H1 event, may indicate spring snowmelt. Future work will determine if vegetation changes play a role in the fluorescent banding reversals. For now, we look to test our interpretations with evidence from other regional and global environmental proxies.

Denton et al. (2010) compile prior work (including Crowley, 1992; Broecker, 1998; Clark et al., 2004; Wang et al., 2006; Toggweiler et al., 2006; Anderson et al., 2009; Cheng et al., 2009) and present an intriguing global-scale model of the last deglaciation from which we can infer seasonality in the EM. In this model, glacial meltwater input to the North Atlantic slows Atlantic Meridional Overturning Circulation, causes the H1 and YD stadials, and induces the spread of winter sea ice in the North Atlantic and severe winters in the Northern Hemisphere. Reduced heat transport to the Northern Hemisphere, a result of the bipolar seesaw (Broecker, 1998), causes the Intertropical Convergence Zone to shift south, which in turn moves atmospheric circulation cells, including the westerlies in both hemispheres, to the south. In the Afro-Asian monsoon region, these changes result in widespread drought during H1 (Stager et al., 2011). In the EM, shifting the Northern Hemisphere westerlies to the south during the H1 and YD events could move these winds and their characteristic weather systems over Soreq Cave and bring moisture to the region on a year-round basis. The sinusoidal fluorescence in sample 2N during both the H1 and YD may indicate year-round rainfall, but it is important to note that this scenario could still result in less total annual rainfall than during the Bølling–Allerød or Holocene. Our snowmelt explanation for bands with "reversed sawtooth" fluorescence (Fig. 2C) also fits the Denton et al. model, although the increased occurrence of this band pattern before 15 ka suggests H1 winters above Soreq had more snowfall than YD winters.

Although it is instructive to test our climate hypotheses against a simplified explanation of the Denton et al. (2010) model, we acknowledge the need for more rigorous tests. Other regional paleoclimate proxies, including both Dead Sea level and pollen records, can potentially contribute to these tests. Drawbacks with these alternative proxies, however, confound any strong conclusions at this time. Ongoing analysis of trace elements in sample 2N will provide more information to evaluate on both millennial and sub-annual timescales, and may further explain hydrologic and vegetation changes. Finally, examining isotope-enabled climate simulations (Schmidt et al., 2007; LeGrande and Schmidt, 2008; Tierney et al., 2011) of the last deglaciation at seasonal resolution may provide additional constraints for our seasonal climate hypotheses, the interpretation of EM climate proxies, and the mechanisms that drive EM climate change.

5. CONCLUSIONS

This study presents the first detailed record of seasonal-scale environmental information from a speleothem that grew during the last deglaciation. The combination of 10 μm-diameter spot analyses of $\delta^{18}O$ by ion microprobe and CLFM imaging allows for the study of sub-domains of individual annual growth bands. The large data set provides new constraints for interpreting climate change at the sub-annual scale. This high-resolution analytical method is ideal for examining both rapid climate change events (e.g., Younger Dryas termination) as well as seasonal climate differences between broad time slices (e.g., Younger Dryas vs. Holocene).

High-precision ion microprobe analyses of $\delta^{18}O$ (0.3‰, 2 s.d., 10 μm-diameter spot) in samples 2N (34–4 ka) and 2-6 (2.2–0.9 ka) show regular fluctuations across fluorescent bands that record seasonal rainfall variability. Calculated values of $|\Delta^{18}O|$, the magnitude of the $\delta^{18}O$ difference within individual annual growth bands, indicate the seasonal character of rainfall. The fluorescent patterns of individual growth bands contribute further to paleoclimate interpretations:

(1) In the Holocene, the ubiquitous sawtooth pattern of both $\delta^{18}O$ and fluorescence variability (Fig. 2A) indicates that the modern seasonal regime of wet winters and dry summers has been consistent since 10.5 ka. Smaller $|\Delta^{18}O|$ values indicate dryer years.
(2) Small values of $|\Delta^{18}O|$ and narrow banding indicate that climate during the Younger Dryas may have been drier than during the Holocene. Sinusoidal intensity of fluorescent banding, however, suggests that dripwater supply from the overlying soil column was more consistent throughout the year than in the Holocene.
(3) The isotope record of the YD termination in sample 2N occurs in multiple stages, which supports the interpretation of cave hydrology presented by Orland et al. (2009). Band-counting across the Younger Dryas termination, constrained by the *in situ* $\delta^{18}O$ data, gives a minimum estimate of 12 years for the isotope shift associated with the hemisphere-wide rapid warming event.
(4) The Heinrich 1 event is characterized by a regular reversal in the fluorescent banding pattern (i.e. dark-before-bright banding) relative to that in the Holocene. Furthermore, the mean $|\Delta^{18}O|$ value during this period is higher than during the YD and Holocene. Decreased seasonal rainfall gradients, regular snow cover, and different overlying vegetation are proposed as possible causes for these observations. The banding patterns and $|\Delta^{18}O|$ values indicate that the modern amount effect – an empirical relationship of annual rainfall $\delta^{18}O$ value to rainfall amount – is unreliable when applied to Soreq Cave speleothems during either Heinrich 1 or the last glacial period.

(5) The fluorescent banding and $|\Delta^{18}O|$ values during the last glacial stadial are most similar to that during Heinrich 1, suggesting comparable climate.

ACKNOWLEDGMENTS

We thank N. Kita for help with ion microprobe set-up and operation; F. He, A. Carlson, S. Meyers, J. Williams and C. Johnson for fruitful conversation and guidance; A. Trzaskus for help with an ion microprobe analysis session; B. Hess, J. Kern, and M. Spicuzza for assistance with sample preparation; L. Rodenkirch for guidance at the Keck Bioimaging Lab at UW-Madison; J. Fournelle and D. Ortiz for guidance at the UW-Madison SEM lab. V. Ersek and two anonymous reviewers provided helpful comments that improved this manuscript. Funding support came from Comer Science and Education Foundation, NSF (AGS-1003487, EAR-0838058), DOE (93ER14389), and the United States-Israel Binational Science Foundation (2010316). WiscSIMS is partially supported by NSF-EAR (0319230, 0744079, 1053466).

APPENDIX A. SUPPLEMENTARY DATA

Supplementary data associated with this article can be found, in the online version, at http://dx.doi.org/10.1016/j.gca.2012.04.035.

REFERENCES

Affek H. P., Bar-Matthews M., Ayalon A., Matthews A. and Eiler J. M. (2008) Glacial/interglacial temperature variations in Soreq cave speleothems as recorded by 'clumped isotope' thermometry. *Geochim. Cosmochim. Acta* **72**, 5351–5360.

Almogi-Labin A., Bar-Matthews M., and Ayalon A. (2004) Climate variability in the Levant and northeast Africa during the Late Quaternary based on marine and land records. In *Human Paleoecology in the Levantine Corridor* (eds. N. Goren-Inbar and J. D. Speth). Oxbow Press, Oxford. pp. 117-134.

Almogi-Labin A., Bar-Matthews M., Shriki D., Kolosovsky E., Paterne M., Schilman B., Ayalon A., Aizenshtat Z. and Matthews A. (2009) Climatic variability during the last ~90 ka of the southern and northern Levantine basin as evident from marine records and speleothems. *Quat. Sci. Rev.* **28**, 2882–2896.

Anderson R. F., Ali A., Bradtmiller L. I., Nielsen S. H. H., Fleisher M. Q., Anderson B. E. and Burckle L. H. (2009) Wind-driven Upwelling in the Southern Ocean and the Deglacial Rise in Atmospheric CO_2. *Science* **323**, 1443–1448.

Atkinson T. C., Briffa K. R. and Coope G. R. (1987) Seasonal temperatures in Britain during the past 22,000 years, reconstructed using beetle remains. *Nature* **325**, 587–592.

Ayalon A., Bar-Matthews M. and Sass E. (1998) Rainfall-recharge relationships within a karstic terrain in the Eastern Mediterranean semi-arid region, Israel: $\delta^{18}O$ and δD characteristics. *J. Hydro.* **207**, 18–31.

Ayalon A., Bar-Matthews M. and Kaufman A. (1999) Petrography, strontium, barium and uranium concentrations, and strontium and uranium isotope ratios in speleothems as palaeoclimatic proxies: Soreq Cave, Israel. *Holocene* **9**, 715–722.

Ayalon A., Bar-Matthews M. and Schilman B. (2004) Rainfall isotopic characteristics at various sites in Israel and the relationships with unsaturated zone water. In *Geological Survey of Israel Reports, GSI/16/04*. The Ministry of National Infrastructures, Jerusalem.

Baker A., Smart P. L., Edwards R. L. and Richards D. A. (1993) Annual growth banding in a cave stalagmite. *Nature* **364**, 518–520.

Baker A., Barnes W. L. and Smart P. L. (1996) Speleothem luminescence intensity and spectral characteristics: signal calibration and a record of palaeovegetation change. *Chem. Geol.* **130**, 65–76.

Baldini J. U. L., McDermott F., Hoffman D. L., Richards D. A. and Clipson N. (2008) Very high-frequency and seasonal cave atmosphere PCO_2 variability: implications for stalagmite growth and oxygen isotope-based paleoclimate records. *Earth Planet. Sci. Lett.* **272**, 118–129.

Banner J. L., Guilfoyle A., James E. W., Stern L. A. and Musgrove M. (2007) Seasonal variations in modern speleothem calcite growth in central Texas, USA. *J. Sed. Res.* **77**, 615–622.

Bard E., Rostek F., Turon J.-L. and Gendreau S. (2000) Hydrological impact of Heinrich Events in the subtropical northeast Atlantic. *Science* **289**, 1321–1324.

Bar-Matthews M. and Ayalon A. (2011) Mid-Holocene climate variations revealed by high-resolution speleothem records from Soreq Cave, Israel and their correlation with cultural changes. *Holocene* **21**, 163–171.

Bar-Matthews M., Ayalon A., Matthews A., Sass E. and Halicz L. (1996) Carbon and oxygen isotope study of the active water-carbonate system in a karstic Mediterranean cave: implications for paleoclimate research in semiarid regions. *Geochim. Cosmochim. Acta* **60**, 337–347.

Bar-Matthews M., Ayalon A. and Kaufman A. (1997) Late Quaternary paleoclimate in the eastern Mediterranean region from stable isotope analysis of speleothems at Soreq Cave, Israel. *Quat. Res.* **47**, 155–168.

Bar-Matthews M., Ayalon A., Kaufman A. and Wasserburg G. J. (1999) The Eastern Mediterranean paleoclimate as a reflection of regional events: Soreq Cave, Israel. *Earth Planet. Sci. Lett.* **166**, 85–95.

Bar-Matthews M., Ayalon A. and Kaufman A. (2000) Timing and hydrological conditions of sapropel events in the Eastern Mediterranean, as evident from speleothems, Soreq cave, Israel. *Chem. Geol.* **169**, 145–156.

Bar-Matthews M., Ayalon A., Gilmour M., Matthews A. and Hawkesworth C. J. (2003) Sea–land oxygen isotopic relationships from planktonic foraminifera and speleothems in the Eastern Mediterranean region and their implication for paleorainfall during interglacial intervals. *Geochim. Cosmochim. Acta* **67**, 3181–3199.

Bar-Matthews M., Marean C. W., Jacobs Z., Karkanas P., Fisher E. C., Herries A. I. R., Brown K., Williams H. M., Bernatchez J., Ayalon A. and Nielssen P. J. (2010) A high resolution and continuous isotopic speleothem record of paleoclimate and paleoenvironment from 90–53 ka from Pinnacle Point on the south coast of South Africa. *Quat. Sci. Rev.* **29**, 2131–2145.

Bartov Y., Goldstein S. L., Stein M. and Enzel Y. (2003) Catastrophic arid episodes in the Eastern Mediterranean linked with the North Atlantic Heinrich events. *Geology* **31**, 439–442.

Baruch U. and Bottema S. (1991) Palynological evidence for climatic changes in the Levant ca. 17,000–9000 B. P. In *The Natufian Culture in the Levant. International Monographs in Prehistory, Archaeological Series 1* (eds. O. Bar-Yosef and F. R. Valla). Ann Arbor, Michigan. pp. 11–20.

Baruch U. and Bottema S. (1999) A new pollen diagram from Lake Hula: vegetational, climatic, and anthropogenic implications. In *Ancient Lakes: Their Cultural and Biological Diversity* (eds.

H. Kawanabe, G. W. Coulter and A. C. Roosevelt). Kenobi Productions, Ghent, pp. 75–86.

Bookman R., Enzel Y., Agnon A. and Stein M. (2004) Late Holocene lake-levels of the Dead Sea. *GSA Bull.* **116**, 555–571.

Bottema S. (1995) The Younger Dryas in the eastern Mediterranean. *Quat. Sci. Rev.* **14**, 883–891.

Broecker W. S. (1998) Paleocean circulation during the last deglaciation: a bipolar seesaw? *Paleocean* **13**, 119–121.

Cheng H., Edwards R. L., Broecker W. S., Denton G. H., Kong X., Wang Y., Zhang R. and Wang X. (2009) Ice age terminations. *Science* **326**, 248–252.

Clark P. U., McCabe A. M., Mix A. C. and Weaver A. J. (2004) Rapid rise of sea level 19,000 years ago and its global implications. *Science* **304**, 1141–1144.

Crowley T. J. (1992) North Atlantic deep water cools the Southern Hemisphere. *Paleocean* **7**, 489–497.

Davidson E. A. and Janssens I. A. (2006) Temperature sensitivity of soil carbon decomposition and feedbacks to climate change. *Nature* **440**, 165–173.

De Lange G. J., Thomson J., Reitz A., Slomp C. P., Principato M. S., Erba E. and Corselli C. (2008) Synchronous basin-wide formation and redox-controlled preservation of a Mediterranean sapropel. *Nature Geo.* **1**, 606–610.

Denton G. H., Alley R. B., Comer G. C. and Broecker W. S. (2005) The role of seasonality in abrupt climate change. *Quat. Sci. Rev.* **24**, 1159–1182.

Denton G. H., Anderson R. F., Toggweiler J. R., Edwards R. L., Schaefer J. M. and Putnam A. E. (2010) The last glacial termination. *Science* **328**, 1652–1656.

Enzel Y., Bookman R., Sharon D., Gvirtzman H., Dayan U., Baruch Z. and Stein M. (2003) Late Holocene climates of the Near East deduced from Dead Sea level variations and modern regional winter rainfall. *Quat. Res.* **60**, 263–273.

Fairchild I. J., Smith C. L., Baker A., Fuller L., Spötl C., Mattey D. and McDermott F. (2006) Modification and preservation of environmental signals in speleothems. *Earth Sci. Rev.* **75**, 105–153.

Frumkin A., Ford D. C. and Schwarcz H. P. (2000) Paleoclimate and vegetation of the last glacial cycles in Jerusalem from a speleothem record. *Glob. Biogeochem. Cycl.* **14**, 863–870.

Hajar L., Khater C. and Cheddadi R. (2008) Vegetation changes during the late Pleistocene and Holocene in Lebanon: a pollen record from the Bekaa Valley. *Holocene* **18**, 1089–1099.

Hendy C. H. (1971) The isotopic geochemistry of speleothems – I. The calculation of the effects of different modes of formation on the isotopic composition of speleothems and their applicability as paleoclimate indicators. *Geochim. Cosmochim. Acta* **35**, 801–824.

IPCC (2007) Climate Change 2007: the physical science basis. Summary for policymakers. Contribution of working group I to the fourth assessment report. The Intergovernmental Panel on Climate Change.

Kallel N., Paterne M., Duplessy J.-C., Vergnaud-Grazzini C., Pujol C., Labeyrie L., Arnold M., Fontugne M. and Pierre C. (1997) Enhanced rainfall in the Mediterranean region during the last sapropel event. *Ocean. Acta* **20**, 697–712.

Kaufman A., Wasserburg G. J., Porcelli D., Bar-Matthews M., Ayalon A. and Halicz L. (1998) U–Th isotope systematics from the Soreq cave, Israel and climatic correlations. *Earth Planet. Sci. Lett.* **156**, 141–155.

Kita N. T., Ushikubo T., Fu B. and Valley J. W. (2009) High precision SIMS oxygen isotope analyses and the effect of sample topography. *Chem. Geol.* **264**, 43–57.

Kolodny Y., Bar-Matthews M., Ayalon A. and McKeegan K. D. (2003) A high spatial resolution $\delta^{18}O$ profile of a speleothem using an ion microprobe. *Chem. Geol.* **197**, 21–28.

Kolodny Y., Stein M. and Machlus M. (2005) Sea-rain-lake relation in the Last Glacial East Mediterranean revealed by $\delta^{18}O$–$\delta^{13}C$ in Lake Lisan aragonites. *Geochim. Cosmochim. Acta* **69**, 4045–4060.

Kozdon R., Ushikubo T., Kita N. T., Spicuzza M. and Valley J. W. (2009) Intratest oxygen isotope variability in the planktonic foraminifer *N. pachyderma:* real vs. apparent vital effects by ion microprobe. *Chem. Geol.* **258**, 327–337.

Kozdon R., Kelly D. C., Kita N. T., Fournelle J. H. and Valley J. W. (2011) Planktonic foraminiferal oxygen isotope analysis by ion microprobe technique suggests warm tropical sea surface temperatures during the Early Paleogene. *Paleocean* **26**, PA3206.

Lachniet M. S. (2009) Climatic and environmental controls on speleothem oxygen-isotope values. *Quat. Sci. Rev.* **28**, 412–432.

Langgut D., Almogi-Labin A., Bar-Matthews M. and Weinstein-Evron M. (2011) Vegetation and climate changes in the South Eastern Mediterranean during the Last Glacial-Interglacial cycle (86 ka): new marine pollen record. *Quat. Sci. Rev.* **30**, 3960–3972.

LeGrande A. N. and Schmidt G. A. (2008) Ensemble, water isotope-enabled, coupled general circulation modeling insights into the 8.2 ka event. *Paleocean* **23**, PA3207.

Lisker S., Vaks A., Bar-Matthews M., Porat R. and Frumkin A. (2009) Stromatolites in caves of the Dead Sea Fault Escarpment: implications to latest Pleistocene lake levels and tectonic subsidence. *Quat. Sci. Rev.* **28**, 80–92.

Marino G., Rohling E. J., Sangiorgi F., Hayes A., Casford J. L., Lotter A. F., Kucera M. and Brinkhuis H. (2008) Early and middle Holocene in the Aegean Sea: interplay between high and low latitude climate variability. *Quat. Sci. Rev.* **28**, 3246–3262.

Matthews A., Ayalon A. and Bar-Matthews M. (2000) D/H ratios of fluid inclusions of Soreq Cave Israel speleothems as a guide to the Eastern Mediterranean Meteoric Line relationships in the last 120 ky. *Chem. Geol.* **166**, 183–191.

McDermott F. (2004) Palaeo-climate reconstruction from stable isotope variations in speleothems: a review. *Quat. Sci. Rev.* **23**, 901–918.

McGarry S. F. and Baker A. (2000) Organic acid fluorescence. applications to speleothem palaeoenvironmental reconstruction. *Quat. Sci. Rev.* **19**, 1087–1101.

McGarry S. F., Bar-Matthews M., Matthews A., Vaks A., Schilman B. and Ayalon A. (2004) Constraints on hydrological and paleotemperature variations in the eastern Mediterranean region in the last 140ka given by the dD values of speleothem fluid inclusions. *Quat. Sci. Rev.* **23**, 919–934.

Mickler P. J., Stern L. A. and Banner J. L. (2006) Large kinetic isotope effects in modern speleothems. *GSA Bull.* **118**, 65–81.

Orland I. J., Bar-Matthews M., Kita N. T., Ayalon A., Matthews A. and Valley J. W. (2009) Climate deterioration in the eastern Mediterranean as revealed by ion microprobe analysis of a speleothem that grew from 2.2 to 0.9 ka in Soreq Cave, Israel. *Quat. Res.* **71**, 27–35.

Rossignol-Strick M. (1995) Sea-land correlation of pollen records in the Eastern Mediterranean for the glacial–interglacial transition: biostratigraphy versus radiometric time-scale. *Quat. Sci. Rev.* **14**, 893–915.

Rossignol-Strick M., Nesteroff W., Olive P. and Vergnaud-Grazzini C. (1982) After the deluge: Mediterranean stagnation and sapropel formation. *Nature* **295**, 105–110.

Rushdi A. I., Clark P. U., Mix A. C., Ersek V., Simoneit B. R. T., Cheng H. and Edwards R. L. (2011) Composition and sources of lipid compounds in speleothem calcite from southwestern Oregon and their paleoenvironmental implications. *Environ. Earth Sci.* **62**, 1245–1261.

Schmidt G. A., LeGrande A. N. and Hoffman G. (2007) Water isotope expressions of intrinsic and forced variability in a coupled ocean–atmosphere model. *J. Geophys. Res.* **112**, D10103.

Scholz D. and Hoffman D. L. (2011) StalAge – an algorithm designed for construction of speleothem age models. *Quat. Geochron.* **6**, 369–382.

Senesi N., Miano T. M., Provenzano M. R. and Brunetti G. (1991) Characterisation, differentiation and classification of humic substances by fluorescence spectroscopy. *Soil Sci.* **152**, 259–271.

Severinghaus J. P., Sowers T., Brook E. J., Alley R. B. and Bender M. L. (1998) Timing of abrupt climate change at the end of the Younger Dryas interval from thermally fractionated gases in polar ice. *Nature* **391**, 141–146.

Stager J. C., Ryves D. B., Chase B. M. and Pausata F. S. R. (2011) Catastrophic drought in the Afro-Asian monsoon region during Heinrich event 1. *Science* **331**, 1299–1302.

Steffensen J. P., Andersen K. K., Bigler M., Clausen H. B., Dahl-Jensen D., Fischer H., Goto-Azuma K., Hansson M., Johnsen S. J., Jouzel J., Masson-Delmotte V., Popp T., Rasmussen S. O., Rothlisberger R., Ruth U., Stauffer B., Siggaard-Andersen M.-L., Sveinbjornsdottir A. E., Svensson A. and White J. W. C. (2008) High-resolution Greenland ice core data show abrupt climate change happens in few years. *Science* **321**, 680–684.

Stein M., Torfstein A., Gavrieli I. and Yechieli Y. (2010) Abrupt aridities and salt deposition in the post-glacial Dead Sea and their North Atlantic connection. *Quat. Sci. Rev.* **29**, 567–575.

Tan M., Baker A., Genty D., Smith C., Esper J. and Cai B. (2006) Applications of stalagmite laminae to paleoclimate reconstructions: comparison with dendrochronology/climatology. *Quat. Sci. Rev.* **25**, 2103–2117.

Taylor K. C., Mayewski P. A., Alley R. B., Brook E. J., Gow A. J., Grootes P. M., Meese D. A., Saltzman E. S., Severinghaus J. P., Twickler M. S., White J. W. C., Whitlow S. and Zielinski G. A. (1997) The holocene-younger dryas transition recorded at Summit, Greenland. *Science* **278**, 825–827.

Tierney J. E., Lewis S. C., Cook B. I., LeGrande A. N. and Schmidt G. A. (2011) Model, proxy and isotopic perspectives on the East African Humid period. *Earth Planet. Sci. Lett.* **307**, 103–112.

Toggweiler J. R., Russell J. L. and Carson S. R. (2006) Midlatitude westerlies, atmospheric CO_2, and climate change during the ice ages. *Paleocean* **21**, PA2005.

Torfstein A., Haase-Schramm A., Waldmann N., Kolodny Y. and Stein M. (2009) U-series and oxygen isotope chronology of the mid = Pleistocene Lake Amora (Dead Sea basin). *Geochim. Cosmochim. Acta* **73**, 2603–2630.

Treble P. C., Schmitt A. K., Edwards R. L., McKeegan K. D., Harrison T. M., Grove M., Chen H. and Wang Y. J. (2007) High resolution SIMS $\delta^{18}O$ analyses of Hulu Cave speleothem at the time of Heinrich event 1. *Chem. Geol.* **238**, 197–212.

Tukey J. W. (1977) *Exploratory Data Analysis*. Addison-Wesley Publishing Co., Reading.

Vaks A., Bar-Matthews M., Ayalon A., Matthews A., Frumkin A., Dayan U., Halicz L., Almogi-Labin A. and Schilman B. (2006) Paleoclimate and location of the border between Mediterranean climate region and the Saharo-Arabian Desert as revealed by speleothems from the northern Negev Desert, Israel. *Earth Planet. Sci. Lett.* **249**, 384–399.

Valley J. W. and Kita N. T. (2005) *First Results from the UW CAMECA IMS-1280*. Fourth Biennial Geochemical SIMS Workshop.

Valley J. W. and Kita N. T. (2009) In situ oxygen isotope geochemistry by ion microprobe. In *MAC Short Course: Secondary Ion Mass Spectrometry in the Earth Sciences*, vol. 41 (ed. M. Fayek). Mineralogical Association of Canada, Toronto. pp. 19–63.

Verheyden S., Nader F. H., Cheng H., Edwards L. R. and Swennen R. (2008) Paleoclimate reconstruction in the Levant region from the geochemistry of a Holocene stalagmite from the Jeita cave, Lebanon. *Quat. Res.* **70**, 368–381.

Waldmann N., Torfstein A. and Stein M. (2010) Northward intrusions of low- and mid-latitude storms across the Saharo-Arabian belt during past interglacials. *Geology* **38**, 567–570.

Wang Y. J., Cheng H., Edwards R. L., An Z. S., Wu J. Y., Shen C.-C. and Dorale J. (2001) A high-resolution absolute-dated late pleistocene monsoon record from Hulu Cave, China. *Science* **294**, 2345–2348.

Wang X., Auler A. S., Edwards R. L., Cheng H., Ito E. and Solheid M. (2006) Interhemispheric anti-phasing of rainfall during the last glacial period. *Quat. Sci. Rev.* **25**, 3391–3403.

Wong C. I., Banner J. L. and Musgrove M. (2011) Seasonal dripwater Mg/Ca and Sr/Ca variations driven by cave ventilation: implications for and modeling of speleothem paleoclimate records. *Geochim. Cosmochim. Acta* **75**, 3514–3529.

Associate editor: James McManus